

Article

In-Plane Libration Suppression of a Two-Segment Tethered Towing System

Shouxu Chen, Weidong Chen, Ti Chen  and Junjie Kang

State Key Laboratory of Mechanics and Control for Aerospace Structures, Nanjing University of Aeronautics and Astronautics, Nanjing 210016, China

* Correspondence: chenti@nuaa.edu.cn

Abstract: A tethered towing system provides an effective method for capturing pieces of space debris and dragging them out of orbit. This paper focuses on the in-plane stability analysis and libration control of a two-segment tethered towing system. The first segment is the same as the traditional single-tether towing system. The second segment is similar to a simplified space tether net. The dynamic equations are established in the orbit frame. Considering the elasticity of the tethers, the equilibrium solutions are obtained and the stability of equilibrium solutions is proved. An in-plane libration controller based on the sliding mode control scheme is designed to ensure the safety of the towing mission and save fuel. The controller suppressed the librations of the in-plane angles in the desired state by applying two external torques. Finally, simulation results are provided to validate the effectiveness of the proposed controller.

Keywords: tether towing system; equilibrium solutions; sliding mode control; libration controller



Citation: Chen, S.; Chen, W.; Chen, T.; Kang, J. In-Plane Libration Suppression of a Two-Segment Tethered Towing System. *Aerospace* **2023**, *10*, 286. <https://doi.org/10.3390/aerospace10030286>

Academic Editor: Andrea Da-Ronch

Received: 8 February 2023

Revised: 8 March 2023

Accepted: 9 March 2023

Published: 13 March 2023



Copyright: © 2023 by the authors. Licensee MDPI, Basel, Switzerland. This article is an open access article distributed under the terms and conditions of the Creative Commons Attribution (CC BY) license (<https://creativecommons.org/licenses/by/4.0/>).

1. Introduction

According to European Space Agency (ESA)'s Space Environment Report 2022, more than 30,000 pieces of space debris have been spotted so far. Active debris removal technology becomes particularly necessary to ensure the safety of human assets in orbit [1]. Scholars have proposed dozens of schemes for removing debris. The use of a space net is an effective technique to remove debris. This method stabilizes the attitude of the captured debris by limiting its degrees of freedom [2]. Botta evaluated the effect of different mechanical models on the simulation of capturing the target using a net from the perspective of dynamic calculation [3]. Simulations have been performed to study target capturing using a space net [4,5]. Sharf et al. presented a space net closing mechanism. Experiments demonstrated the practicality of the net closing system [6]. Yue established the dynamic model of a rectangular space net and validated its accuracy by comparing it with on-ground experiments [7]. For active debris removal technology, Lv et al. proposed an integrated platform scheme [8].

A tethered towing system (TTS) is an active space debris removal technology derived from the tethered satellite system (TSS). TTS has become another one of the most likely solutions to the large debris deorbit due to its simple structure, light weight, low cost, variable system structural parameters, and large capture distance [9]. Stadnyk proposed a new tether model using a spring-damper element to simulate the target capture process [10]. Many studies have been carried out on the system dynamic analysis [11,12]. Abouelmagd studied the dynamic problem considering the effect of the zonal harmonic parameter [13]. Pang et al. studied the nonlinear dynamics of a TSS in the orbital plane and obtained the analytical solutions of internal resonance [14]. Aslanov and Ledkov studied the dynamic influence of the atmosphere on a TTS [15]. Later, Aslanov and Yuditsev studied the coupling dynamics between tether vibration and flexible attachment vibration when a TTS towed space debris with flexible attachments [16]. Then, they took the target with fuel

residue as the research object and studied the influence of attitude motion of such objects on the safety of the towing process [17]. Aslanov et al. analyzed the balanced configuration and stability of the system and proposed guidelines for selecting appropriate thrust, tug mass, and tether length to avoid chaotic motion [18]. Aslanov and Yudinsev found that if the tether was connected off-center to the debris, shifting the orbit by changing the thrust would increase the pitch oscillations of the tether, ultimately leading to the chaotic motion of the system [19]. Aslanov also studied the stability of pendulum systems with moving mass blocks near the equilibrium position [20]. By considering the large deformation of a tether, Lim calculated the dynamic responses of a TTS for the variations of the capture angles and capture velocities of the debris, and the effects of varying system parameters were analyzed [21]. Shan performed modal analysis for a TTS and derived an analytical solution of the system's natural frequency. The influence of the initial angular velocity of the target on the chaser satellite was analyzed [22].

Regarding the tether structures, Qi proposed a double-tether TTS, in which the tethers were connected to the edge of the debris [23]. Hovell proposed a bifurcated TTS and studied the system stability when capturing a non-cooperative failed spacecraft in the orbital environment [24–26]. Then the planar experiments were carried out. The results showed that the proposed system better exploited tether damping and improved despinning performance as compared to the single-tether configuration [27]. Yang et al. proposed a sub-tether configuration of a TTS and performed some simulations to demonstrate the effectiveness of the proposed system [28]. Shan compared the single-tether configuration and the sub-tether configuration based on three models, namely the modified dumbbell model, the lumped-mass model, and the ANCF model [22]. The sub-tether configuration provides a new way for active debris removal technology, which acquires the advantages of the space net and the TTS. However, it may exhibit more different dynamics behavior than the traditional single-tether configuration.

In terms of stability analysis, Abouelmagd et al. studied the positions of the equilibria points and their stability for a dumbbell satellite when the central body is an oblate spheroid [29]. Qi studied the equilibrium solutions and their stability for a TTS and proposed two feedback control schemes to stabilize the debris attitude [23]. Considering the debris as a flexible beam, Hu found that the mass ratio between the tug and the debris determines the equilibrium solutions and the reach time [30]. Lian et al. studied the chaotic motion and control problems using Melnikov's method and proposed a chaotic control method based on an inertia damper [31]. Liu found that by increasing tether damping, the system motion could be stabilized near the equilibrium points and the quasi-periodic motion could be changed into periodic motion [32]. Sun and Zhao found that the mass of the main satellite had a significant influence on the stability and libration characteristics [33].

In terms of system control, Jin and Hu converted the optimal control problem into a linear programming problem by truncating the Chebyshev series and using the quasi-linearization method [34]. For the variable mass of the satellite, Sun et al. proposed a thrust control law using double-switching-type constant thrust [35]. Wen et al. proposed a tension control law based on potential energy shaping and damping injection with only the feedback of the tether length [36]. Zhang et al. designed an algorithm to stabilize TTS with a rotating target by controlling the position of the tug and the tether tension [37]. In order to enhance the robustness of the system, Yang et al. established a three-dimensional dynamic model. When the failed spacecraft had an initial angular velocity, the system could be stabilized by the tether connection point bias control method and tether length control [38]. Kang et al. proposed three control strategies to control a rotating uncooperative target with bounded stability. The effectiveness was validated experimentally using a microgravity platform with two tethered free-floating air-bearing satellite simulators [39].

Sliding mode control, which can overcome uncertainty and has strong robustness to interference, is especially suitable for nonlinear systems, and TTS is a typical nonlinear system. Razzaghi applied an adaptive sliding mode and the state-dependent Riccati equation control method on a TSS [40]. Chu added a time-varying control tension using a

hierarchical sliding mode controller to implement the hybrid control of the in-plane angle and the relative distance [41]. Xu et al. developed a novel fractional-order fuzzy sliding mode control strategy and derived a fuzzy control law in analytical form, which could perform a faster and smoother deployment [42,43]. Kang et al. proposed a fractional order sliding mode control for the deployment, which consisted of two sub-sliding manifolds that were defined separately for the actuated and unactuated states [44]. Li presented a novel discrete-time pure-tension sliding mode predictive control scheme, which inherited the property of explicitly handling constraints from model predictive control and the remarkable robustness of sliding mode control [45]. Li developed a novel fractional-order nonsingular terminal sliding mode control scheme to stabilize an underactuated deployment mission with only tension regulation [46]. Then he investigated a super-twisting sliding mode controller to accelerate the convergence speed of system states and an adaptive law to handle the adverse effect of uncertainty and external disturbance [47]. Liu proposed a robust adaptive control strategy to solve the problem of attitude tracking control for a clean platform, and this control strategy is based on the coupling of the fuzzy logic system with sliding mode control [48]. Researchers have designed many sliding mode control schemes to realize the deployment of TSSs. However, works about suppressing a TTS's in-plane libration are few.

This paper aims to solve the equilibrium configurations of a two-segment tethered towing system and design a controller to suppress the librations of in-plane angles by referring to previous studies. In contrast with the available literature, the contributions of the paper are as follows:

- (1) With the elasticity of the tethers, the equilibrium configurations of a two-segment tethered towing system with constant thrust are obtained and the stabilities of equilibria are proved.
- (2) An in-plane sliding mode controller is designed to suppress the librations of the in-plane angles of the system.

The rest of the paper is organized as follows: Section 2 describes the system composition and gives the dynamic formulations. In Section 3, the three-dimensional dynamic equations are simplified, and the equilibria and stability of the simplified model are studied. In Section 4, a libration controller is designed with the equilibrium solutions as the desired state. In Section 5, the system dynamic characteristics and the effectiveness of the designed controller are simulated. Conclusions are drawn in Section 6.

2. Problem Formulation

The two-segment tether towing system studied in this paper is shown in Figure 1. The system consists of a tug, a sub-satellite, a piece of space debris, and two segments of elastic tethers. The sub-satellite is released by the tug, and the second segment tethers are released by the sub-satellite to capture the space debris. Both the tug and the debris are regarded as rigid bodies. The sub-satellite, whose size is small compared to the length of the tether, can be regarded as a particle. The two parts of the tethers are regarded as massless spring-damper systems and can only be tensioned. The first part is released by the tug. The second part, which is attached to the ends of the debris, is released by the sub-satellite. To describe the kinematic relations of the components accurately, three right-handed frames are introduced. The orbit frame $F_o(o_o x_o y_o z_o)$ has its origin o_o located at the mass center of the tug. The x_o -axis points away from the Earth's center to o_o , the y_o -axis is the flight direction of the tug, and the z_o -axis conforms to the right-handed rule. The tug body frame $F_{B1}(o_{b1} x_{b1} y_{b1} z_{b1})$ and the debris body frame $F_{B2}(o_{b2} x_{b2} y_{b2} z_{b2})$ are placed at the mass centers of the tug and debris, respectively, whose axes are aligned with the principal moments of inertia axes of the two bodies.

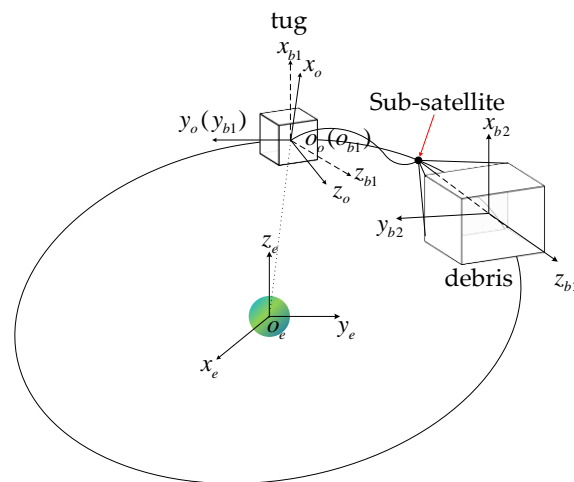


Figure 1. Geometry of the two-segment tether towing system.

The generalized coordinate vector of the system in the orbit frame is selected as

$$X = [D_1 \quad D_2 \quad \vartheta_1 \quad \vartheta_2] \tag{1}$$

where D_1 is the position vector which points from the mass center of the tug to the sub-satellite. D_2 is the position vector which points from the sub-satellite to the mass center of the debris. ϑ_1 and ϑ_2 are the attitude angles.

According to Kane’s method [28], the three-dimensional dynamic equation in the orbit frame can be derived as follows:

$$\ddot{D}_1 + 2\omega_o \times \dot{D}_1 + \omega_o \times D_1 \times \omega_o + D_1 \times \dot{\omega}_o = F_{ex3}/m_3 - F_{ex1}/m_1 \tag{2}$$

$$\ddot{D}_2 + 2\omega_o \times \dot{D}_2 + \omega_o \times D_2 \times \omega_o + D_2 \times \dot{\omega}_o = F_{ex2}/m_2 - F_{ex3}/m_3 \tag{3}$$

$$J_1 \dot{\omega}_{b1}^b + \omega_{b1}^b \times J_1 \omega_{b1}^b = M_{ex1} \tag{4}$$

$$J_2 \dot{\omega}_{b2}^b + \omega_{b2}^b \times J_2 \omega_{b2}^b = M_{ex2} \tag{5}$$

where m_1 is the mass of tug. m_2 is the mass of debris. m_3 is the mass of sub-satellite. ω_{b1}^b and ω_{b2}^b are the rotational angular velocities of the body frames with respect to the orbit frame. ω_o is the orbital angular velocity. J_1 and J_2 are the inertia matrices of tug and debris, respectively. $F_{ex1} = F_{g1} + F_{l1} + F_t$. $F_{ex2} = F_{g2} + F_{l2}$. $F_{ex3} = F_{g3} - F_{l1} - F_{l2}$. $M_{ex1} = M_{g1} + M_{l1} + M_{c1}$. $M_{ex2} = M_{g2} + M_{l2} + M_{c2}$. F_{l1} is the tension of the first-part tether. F_{l2} is the tension of the second part ones. F_{gi} and M_{gi} are the force and moment caused by the gravity gradient force. M_{ci} is the control moment.

The tethers are considered as spring-damper systems [10]. The tether material is assumed to have a linear spring constant k_i , a damping coefficient c_i , and unstretched length l_{i0} . The tether force is given as follows:

$$F_{li} = \begin{cases} k_i(\|L_i\| - l_{i0})L_i + c_i d l_i L_i & , \|L_i\| > l_{i0} \\ 0 & , \|L_i\| \leq l_{i0} \end{cases} \tag{6}$$

where L_i is the direction vector of each tether and l_i is the unit vector along the tether.

The three-dimensional dynamics described by Equations (2)–(5) are too complicated, which is not suitable for the stability analysis. Hence, the following assumptions are made to simplify the system in the orbital plane: (1) Ignoring rigid body attitude, the tug, the sub-satellite, and the debris are all regarded as particles. (2) The system operates in an ideal Keplerian orbit. (3) The tethers in the second segment are simplified into an equivalent tether. Its physical coefficient is equal to the sum of all second-part tethers. (4) The out-of-plane orbit motion of the system is ignored.

Figure 2 shows the simplified system schematic diagram. d_1 is the distance between the tug and the sub-satellite. d_2 is the distance between the sub-satellite and the debris. θ_1 is the in-plane angle between the first-part tether and the negative direction of the x_o -axis. θ_2 is the in-plane angle between the equivalent tether and the negative direction of the x_o -axis. F_t is the thrust of the tug. γ is the angle between the thrust and the y_o -axis.

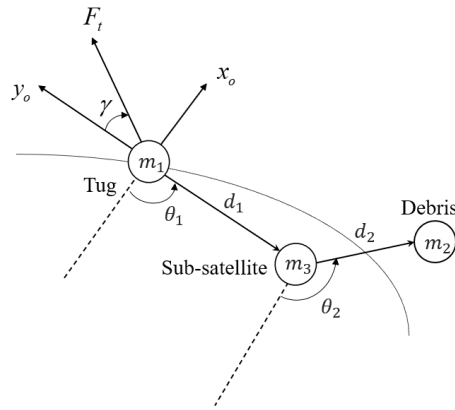


Figure 2. Schematic diagram of simplified system model.

Based on Equation (1) and the assumptions, the generalized coordinate of the simplified system is $\mathbf{X}_s = [d_1 \ d_2 \ \theta_1 \ \theta_2]$. The dimensionless transformation relation is introduced as follows:

$$\bar{F}_i = \frac{F_i}{m_1 \omega_0^2 d_{10}} \tag{7}$$

$$(\)' = \frac{d(\)}{df} = \frac{1}{\omega_0} \frac{d(\)}{dt} \tag{8}$$

where the superscript “()’” indicates differentiation with respect to the true anomaly f . Employing the transformations yields the following dimensionless dynamic equations

$$d_1'' = d_1(\theta_1' + 1)^2 - d_1(1 - 3 \cos^2 \theta_1) - \mu_1 d_{10} \bar{F}_{l1} + \mu_3 d_{10} \bar{F}_{l2} \cos(\theta_2 - \theta_1) + \bar{F}_t d_{10} \sin(\theta_1 + \gamma) \tag{9}$$

$$d_2'' = d_2(\theta_2' + 1)^2 - d_2(1 - 3 \cos^2 \theta_2) - \mu_2 d_{10} \bar{F}_{l2} + \mu_3 d_{10} \bar{F}_{l1} \cos(\theta_2 - \theta_1) \tag{10}$$

$$\theta_1'' = -\frac{3}{2} \sin 2\theta_1 - 2 \frac{d_1'}{d_1} (\theta_1' + 1) + \mu_3 \frac{d_{10} \bar{F}_{l2}}{d_1} \sin(\theta_2 - \theta_1) + \frac{d_{10} \bar{F}_t}{d_1} \cos(\theta_1 + \gamma) \tag{11}$$

$$\theta_2'' = -\frac{3}{2} \sin 2\theta_2 - \frac{\mu_3 d_{10} \bar{F}_{l1}}{d_2} \sin(\theta_2 - \theta_1) - 2 \frac{d_2'}{d_2} (\theta_2' + 1) \tag{12}$$

where μ_1, μ_2 , and μ_3 are dimensionless constants defined as follows:

$$\mu_1 = \frac{(m_1 + m_3)m_1}{m_1 m_3}, \mu_2 = \frac{(m_2 + m_3)m_1}{m_2 m_3}, \mu_3 = \frac{m_1}{m_3} \tag{13}$$

3. Equilibria and Stability Analysis

3.1. Equilibrium Configurations of the System

In order to ensure the stability of the towing process, it is necessary to figure out the equilibrium configurations of the system with constant thrust. To obtain the equilibrium configurations, the derivative terms of d_1, d_2, θ_1 , and θ_2 are set to zero in Equations (9)–(12). One obtains

$$3d_1 \cos^2 \theta_1 - \mu_1 d_{10} \bar{d}_{l1} + \mu_3 d_{10} \bar{F}_{l2} \cos(\theta_2 - \theta_1) + \bar{F}_t d_{10} \sin(\theta_1 + \gamma) = 0 \tag{14}$$

$$3d_2 \cos^2 \theta_2 - \mu_2 d_{10} \bar{F}_{l2} + \mu_3 d_{10} \bar{F}_{l1} \cos(\theta_2 - \theta_1) = 0 \tag{15}$$

$$-\frac{3}{2} \sin 2\theta_1 + \mu_3 \frac{d_{10} \bar{F}_{l2}}{d_1} \sin(\theta_2 - \theta_1) + \frac{d_{10} \bar{F}_t}{d_1} \cos(\theta_1 + \gamma) = 0 \tag{16}$$

$$-\frac{3}{2} \sin 2\theta_2 - \frac{\mu_3 d_{10} \bar{F}_{11}}{d_2} \sin(\theta_2 - \theta_1) = 0 \tag{17}$$

According to Equations (14) and (15), the relationship between \bar{F}_{li} and \bar{F}_t can be given by

$$\bar{F}_{11} = \frac{\mu_2(3d_1 \cos^2 \theta_1 + \bar{F}_t d_{10} \sin(\theta_1 + \gamma)) + 3\mu_3 d_2 \cos^2 \theta_2 \cos(\theta_2 - \theta_1)}{(\mu_1 \mu_2 - \mu_3^2 \cos^2(\theta_2 - \theta_1)) d_{10}} \tag{18}$$

$$\bar{F}_{12} = \frac{3d_2}{\mu_2 d_{10}} \cos^2 \theta_2 + \frac{\mu_3}{\mu_2} \bar{F}_{11} \cos(\theta_2 - \theta_1) \tag{19}$$

When $\gamma = 0$, the direction of the thrust is along the y_o -axis. The solution to Equations (16) and (17) is given as

$$E_1 : \theta_{1e} = \pi/2, \theta_{2e} = \pi/2 \tag{20}$$

In the equilibrium configuration E_1 , the three masses remain in a straight line along the y_o -axis (local horizontal). Combined with Equation (6), $\theta_{1e} = \pi/2$ and $\theta_{2e} = \pi/2$ are substituted into Equations (14) and (15). The equilibrium solutions for tether length can be obtained as follows:

$$d_{1e} = \frac{\mu_2 \bar{F}_t}{(\mu_1 \mu_2 - \mu_3^2) k_1} + d_{10} \tag{21}$$

$$d_{2e} = \frac{\mu_3 k_1 (d_{1e} - d_{10})}{\mu_2 k_2} + d_{20} \tag{22}$$

As shown in Equations (21) and (22), d_{1e} is affected by the thrust. The value of d_{2e} is related to the first-part tether length.

Let $\gamma \neq 0$; the solutions to Equations (16) and (17) are

$$\begin{aligned} E_2 : \theta_{1e} &= \frac{\pi}{2}, \theta_{2e} = \frac{\pi}{2}, E_3 : \theta_{1e} = \frac{\pi}{2}, \theta_{2e} = \arcsin\left(\frac{\mu_2 \mu_3 d_{10} \bar{F}_t \cos \gamma}{3(\mu_1 \mu_2 - \mu_3^2) d_{2e}}\right) \\ E_4 : \theta_{1e} &= 0, \theta_{2e} = 0/\pi, E_5 : \theta_{1e} = 0, \theta_{2e} = \arccos\left(\frac{-3\mu_3 d_1 - \mu_3 d_{10} \bar{F}_t \sin \gamma}{3\mu_1 d_{2e}}\right) \\ E_6 : \theta_{1e} &= \pi, \theta_{2e} = 0/\pi, E_7 : \theta_{1e} = \pi, \theta_{2e} = \arccos\left(\frac{\mu_3 d_1 - \mu_3 d_{10} \bar{F}_t \sin \gamma}{3\mu_1 d_{2e}}\right) \end{aligned} \tag{23}$$

In the configuration E_2 , the three masses remain in the same state as the configuration E_1 . In the configurations E_4 and E_6 , the three masses line up on the x_o -axis (local vertical). The equilibrium solution θ_{2e} in the configurations E_3 , E_5 , and E_7 is determined by γ , d_{1e} , and d_{2e} and can be solved in the same way as in E_1 .

Figure 3 gives the schematic diagrams of the solutions shown in Equation (23). The red ball represents the tug, the light blue ball represents the sub-satellite, and the other balls correspond to the debris in each configuration.

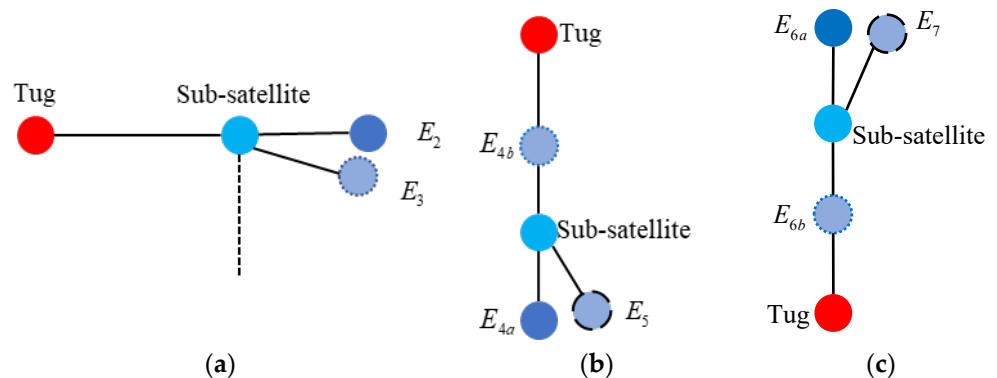


Figure 3. Schematic diagram of the solutions shown in Equation (23): (a) E_2 and E_3 ; (b) E_4 and E_5 ; (c) E_6 and E_7 .

3.2. Stability of Equilibrium Configuration

Define $x = [x_1, x_2, x_3, x_4]^T$, where $x_1 = \theta_1 - \theta_{1e}$, $x_2 = \theta'_1$, $x_3 = \theta_2 - \theta_{2e}$ and $x_4 = \theta'_2$. The new coordinates x represent the variations of θ_1 and θ_2 from their equilibrium solutions. The new equilibrium solutions are $x_e = [0, 0, 0, 0]^T$. Then Equations (16) and (17) can be linearized about x_{1e} and x_{2e} as follows:

$$\begin{cases} \dot{x}_1 = x_2 \\ \dot{x}_2 = C_1x_1 + C_2x_3 \\ \dot{x}_3 = x_4 \\ \dot{x}_4 = C_3x_1 + C_4x_3 \end{cases} \tag{24}$$

where C_i are constants defined as follows:

$$\begin{aligned} C_1 &= -3 \cos 2\theta_{1e} - \mu_3 \frac{d_{10}}{d_{1e}} \bar{F}_{12} \cos(\theta_{2e} - \theta_{1e}) - \bar{F}_t \frac{d_{10}}{d_{1e}} \sin(\theta_{1e} + \gamma), \\ C_2 &= \mu_3 \frac{d_{10}}{d_{1e}} \bar{F}_{12} \cos(\theta_{2e} - \theta_{1e}), \\ C_3 &= \mu_3 \frac{d_{10}}{d_{2e}} \bar{F}_{11} \cos(\theta_{2e} - \theta_{1e}), \\ C_4 &= -3 \cos 2\theta_{2e} - \frac{\mu_3 d_{10}}{d_{2e}} \bar{F}_{11} \cos(\theta_{2e} - \theta_{1e}) \end{aligned} \tag{25}$$

Equation (24) is rewritten in matrix form as follows:

$$\dot{x} = Cx = \begin{bmatrix} 0 & 1 & 0 & 0 \\ C_1 & 0 & C_2 & 0 \\ 0 & 0 & 0 & 1 \\ C_3 & 0 & C_4 & 0 \end{bmatrix} \begin{bmatrix} x_1 \\ x_2 \\ x_3 \\ x_4 \end{bmatrix} \tag{26}$$

The characteristic equation can be obtained as

$$a_0\lambda^4 + a_1\lambda^3 + a_2\lambda^2 + a_3\lambda + a_4 = 0 \tag{27}$$

where $a_0 = 1$, $a_1 = 0$, $a_2 = -(C_1 + C_4)$, $a_3 = 0$, and $a_4 = C_1C_4 - C_2C_3$. It can be found that a_1 and a_3 are zeros for equilibrium configuration. This implies that there is no asymptotic stable equilibrium. There can be marginal stability with imaginary values for all λ_i , provided that $a_0 > 0$, $a_2 > 0$, $a_4 > 0$, and $a_2^2 > 4a_0a_4$.

By solving Equation (22), the eigenvalues can be obtained:

$$\begin{aligned} \lambda_{1,2} &= \pm \sqrt{\frac{C_1}{2} + \frac{C_4}{2} - \frac{\sqrt{(C_1 - C_4)^2 + 4C_2C_3}}{2}} \\ \lambda_{3,4} &= \pm \sqrt{\frac{C_1}{2} + \frac{C_4}{2} + \frac{\sqrt{(C_1 - C_4)^2 + 4C_2C_3}}{2}} \end{aligned} \tag{28}$$

The system physical parameters are set as follows:

$$\begin{aligned} m_1 &= 500 \text{ kg}, m_2 = 2000 \text{ kg}, m_3 = 8 \text{ kg}, F_t = 150 \text{ N} \\ d_{10} &= 100 \text{ m}, d_{20} = 8.5 \text{ m}, k_i = 264 \text{ N/m}, c_i = 8 \text{ Ns/m} \end{aligned} \tag{29}$$

The orbit altitude of the system is 700 km. In E_1 , it can be shown that $a_0 = 1$, $a_2 > 0$, and $a_4 > 0$. It can also be shown that $a_2^2 > 4a_0a_4$. One can determine λ_i as follows:

$$\begin{aligned} \lambda_1 &= 35.1074i, \lambda_2 = -35.1074i, \\ \lambda_3 &= -2.7534 \times 10^{-14} + 5.1636 \times 10^2i, \\ \lambda_4 &= -2.7534 \times 10^{-14} - 5.1636 \times 10^2i \end{aligned} \tag{30}$$

As can be seen from Equation (30), λ_i and λ_i are on the imaginary axis, but they are not multiple roots. There are no roots of the Jodan form; the equilibrium point is stable according to Theorem 4.5 [49].

Considering $\gamma = 1$, it can be shown that $a_0 = 1$, $a_2 > 0$, $a_4 > 0$, and $a_2^2 > 4a_0a_4$ in the line configurations E_2 and $E_{4a}(\theta_{1e} = 0, \theta_{2e} = 0)$. Similar to E_1 , they are also the stability conditions. Taking $E_{4a}(\theta_{1e} = 0, \theta_{2e} = 0)$ as an example, one can determine the λ_i as follows:

$$\begin{aligned} \lambda_1 &= 32.2957i, \lambda_2 = -32.2957i, \\ \lambda_3 &= -2.1316 \times 10^{-14} + 4.5799 \times 10^2i, \\ \lambda_4 &= -2.1316 \times 10^{-14} - 4.5799 \times 10^2i \end{aligned} \tag{31}$$

However, the configurations $E_{4b}(\theta_{1e} = 0, \theta_{2e} = \pi)$ and E_6 do not satisfy the stability condition because the corresponding eigenvalues have real roots. Hence, these equilibriums are unstable.

In configurations $E_3, E_5,$ and $E_7,$ it can be shown that $a_0 = 1, a_2 > 0,$ and $a_4 > 0.$ It can also be shown that $a_2^2 > 4a_0a_4.$ Hence, the equilibrium is stable. One can determine the λ_i as follows:

$$\begin{aligned} \lambda_1 &= 47.6853i, \lambda_2 = -47.6853i, \\ \lambda_3 &= -1.5632 \times 10^{-13} + 1.2312 \times 10^3i, \\ \lambda_4 &= -1.5632 \times 10^{-13} - 1.2312 \times 10^3i \end{aligned} \tag{32}$$

Taking E_1 as an example, it can be obtained that $F_{11e} = 120.096 \text{ N}, F_{12e} = 119.617 \text{ N}, d_{1e} = 100.487 \text{ m},$ and $d_{2e} = 8.9869 \text{ m}$ when the system is stable by substituting the parameters in Equation (29) into Equations (18), (19), (21) and (22). The analysis results are verified by simulation in Section 5.1.

4. Libration Controller Design

In this section, based on the sliding mode control scheme, a controller of in-plane libration angles is designed. The equilibrium solution solved in Section 3 is taken as the desired state. In towing mission, the angles will lead to serious tether librations, which will cause the system configuration to change continuously. To overcome the change, more fuel is required to complete a predetermined mission than the desired state. So, it is desirable for the in-plane libration angles to be maintained at the state to save fuel and ensure mission safety. It is assumed that the tug and the sub-satellite are equipped with air jets that can be used to adjust their positions. The in-plane libration angles can be suppressed to the desired state and maintained at equilibrium by applying external torques. Adding the control inputs into Equations (11) and (12) yields

$$\theta_1'' = -\frac{3}{2} \sin 2\theta_1 - 2\frac{d_1'}{d_1}(\theta_1' + 1) + \frac{m_1 d_{10} \bar{F}_{l2}}{m_3 d_1} \sin(\theta_2 - \theta_1) + \frac{d_{10} \bar{F}_t}{d_1} \cos \theta_1 + u_1 \tag{33}$$

$$\theta_2'' = -\frac{3}{2} \sin 2\theta_2 - \frac{m_1 d_{10} \bar{F}_{l1}}{m_3 d_2} \sin(\theta_2 - \theta_1) - 2\frac{d_2'}{d_2}(\theta_2' + 1) + u_2 \tag{34}$$

Equations (33) and (34) are rewritten in general form as follows:

$$\theta_1' = f_1(\theta_1, \theta_2) + u_1 + d_{dis1} \tag{35}$$

$$\theta_2' = f_2(\theta_1, \theta_2) + u_2 + d_{dis2} \tag{36}$$

where

$$f_1(\theta_1, \theta_2) = -\frac{3}{2} \sin 2\theta_1 + \frac{m_1 \bar{F}_{l2}}{m_3} \sin(\theta_2 - \theta_1) + \bar{F}_t \cos \theta_1 \tag{37}$$

$$f_2(\theta_1, \theta_2) = -\frac{3}{2} \sin 2\theta_2 - \frac{m_1 d_1 \bar{F}_{l1}}{m_3 d_2} \sin(\theta_2 - \theta_1) \tag{38}$$

$$d_{dis1} = -2\frac{d_1'}{d_1}(\theta_1' + 1) \tag{39}$$

$$d_{dis2} = -2\frac{d_2'}{d_2}(\theta_2' + 1) \tag{40}$$

where d_{dis1} and d_{dis2} are time-varying, related to the values of $d_1, d_2, d_1', d_2', \theta_1',$ and $\theta_2'.$ Assume $|d_{dis1}| \leq D_1$ and $|d_{dis2}| \leq D_2,$ in which D_1 and D_2 are positive constants.

Define $\varepsilon_{\theta_1} = \theta_1 - \theta_{1d}$ and $\varepsilon_{\theta_2} = \theta_2 - \theta_{2d}.$ Design sliding surfaces as follows:

$$s_1 = \dot{\varepsilon}_{\theta_1} + c_{s1} \varepsilon_{\theta_1} \tag{41}$$

$$s_2 = \dot{\varepsilon}_{\theta_2} + c_{s2}\varepsilon_{\theta_2} \quad (42)$$

By taking the first derivative of Equations (41) and (42), we obtain

$$\dot{s}_1 = \ddot{\varepsilon}_{\theta_1} + c_{s1}\dot{\varepsilon}_{\theta_1} = \theta_1'' + c_{s1}\theta_1' \quad (43)$$

$$\dot{s}_2 = \ddot{\varepsilon}_{\theta_2} + c_{s2}\dot{\varepsilon}_{\theta_2} = \theta_2'' + c_{s2}\theta_2' \quad (44)$$

The exponential reaching law is adopted to drive the system to the sliding mode surface

$$\dot{s} = -ks - \varepsilon \text{sgns} \quad (45)$$

where $k > 0$ and $\varepsilon > 0$. By combining Equation (45) with Equations (43) and (44), the in-plane libration angle control forces can be designed as

$$u_1 = -k_{s1}s_1 - \varepsilon_{s1}\text{sgns}_1 - c_{s1}\theta_1' - f_1 \quad (46)$$

$$u_2 = -k_{s2}s_2 - \varepsilon_{s2}\text{sgns}_2 - c_{s2}\theta_2' - f_2 \quad (47)$$

with

$$\dot{\varepsilon}_{s_i} = \sigma_i |s_i| \quad (48)$$

where σ_i is a positive constant.

Define $s = [s_1, s_2]^T$. Choose the following Lyapunov function candidate

$$V = \frac{1}{2} s^T s + \frac{1}{2\sigma_{s1}} (\varepsilon_{s1} - D_1)^2 + \frac{1}{2\sigma_{s2}} (\varepsilon_{s2} - D_2)^2 \quad (49)$$

whose time derivative is

$$\dot{V} = s^T \dot{s} + \frac{\dot{\varepsilon}_{s1}}{\sigma_{s1}} (\varepsilon_{s1} - D_1) + \frac{\dot{\varepsilon}_{s2}}{\sigma_{s2}} (\varepsilon_{s2} - D_2) \quad (50)$$

Due to $\dot{\varepsilon}_{s_i} = \sigma_i |s_i|$, we obtain

$$\dot{V} = s_1 \dot{s}_1 + s_2 \dot{s}_2 + (\varepsilon_{s1} - D_1) |s_1| + (\varepsilon_{s2} - D_2) |s_2| \quad (51)$$

Combined with Equations (35), (36), (43) and (44), Equation (51) can be reformulated as

$$\begin{aligned} \dot{V} &= s_1(f_1 + u_1 + d_{dis1} + c_{s1}\theta_1') + s_2(f_2 + u_2 + d_{dis2} + c_{s2}\theta_2') + (\varepsilon_{s1} - D_1) |s_1| + (\varepsilon_{s2} - D_2) |s_2| \\ &= s_1(-k_{s1}s_1 - \varepsilon_{s1}\text{sgns}_1) + s_2(-k_{s2}s_2 - \varepsilon_{s2}\text{sgns}_2) + s_1 d_{dis1} + s_2 d_{dis2} + (\varepsilon_{s1} - D_1) |s_1| + (\varepsilon_{s2} - D_2) |s_2| \\ &= -k_{s1}s_1^2 - k_{s2}s_2^2 + s_1 d_{dis1} + s_2 d_{dis2} - D_1 |s_1| - D_2 |s_2| \end{aligned} \quad (52)$$

In terms of $|d_{dis1}| \leq D_1$ and $|d_{dis2}| \leq D_2$, we obtain

$$\begin{aligned} s_1 d_{dis1} - D_1 |s_1| &\leq 0 \\ s_2 d_{dis2} - D_2 |s_2| &\leq 0 \end{aligned} \quad (53)$$

Thus,

$$\dot{V} \leq -k_{s1}s_1^2 - k_{s2}s_2^2 \quad (54)$$

When $s \neq [0, 0]^T$, it is clear that \dot{V} is negative. Hence, the system will converge to the sliding surface and reach the equilibrium asymptotically along the sliding surface. Therefore, the in-plane libration angles could converge to the desired state with u_1 and u_2 .

5. Simulation Results

To verify the results of theoretical analysis and the effectiveness of the designed controller, simulations are carried out with initial physical parameters shown in Equation (29). The simulation results of the equilibrium configuration E_1 are shown in Section 5.1. Those of the system with control are shown in Section 5.2.

5.1. Simulations for Equilibrium Configuration

In the following simulation, it is assumed that the initial state deviates from the equilibrium state and the tethers are tensioned. The physical parameters shown in Equation (29) and the initial values $[d_1, d'_1, \theta_1, \theta'_1, d_2, d'_2, \theta_2, \theta'_2] = [100.1, 0, 1.5, 0, 8.7, 0, 1.4, 0]$ are used for the numerical simulation of Equations (9)–(12). The results are shown as follows:

Figure 4 shows the variations of the generalized coordinate X_s . It can be found that d_1 and d_2 show large libration amplitudes, which are driven by d_{dis1} and d_{dis2} , and their maximum values are 100.621 and 9.121. Since the initial condition deviates from the configuration E_1 and the tether is tensioned, the tether length will change at the beginning, so that d'_1 and d'_2 are non-zero and d_{dis1} and d_{dis2} occur. When the system reaches the equilibrium state at $f = 0.8$, the tether length and the other coordinates tend to be stable. The equilibrium positions of d_1 and d_2 are equal to 100.487 and 8.9869, respectively, while those of θ_1 and θ_2 are equal to $\pi/2$, which is in good agreement with the analysis results.

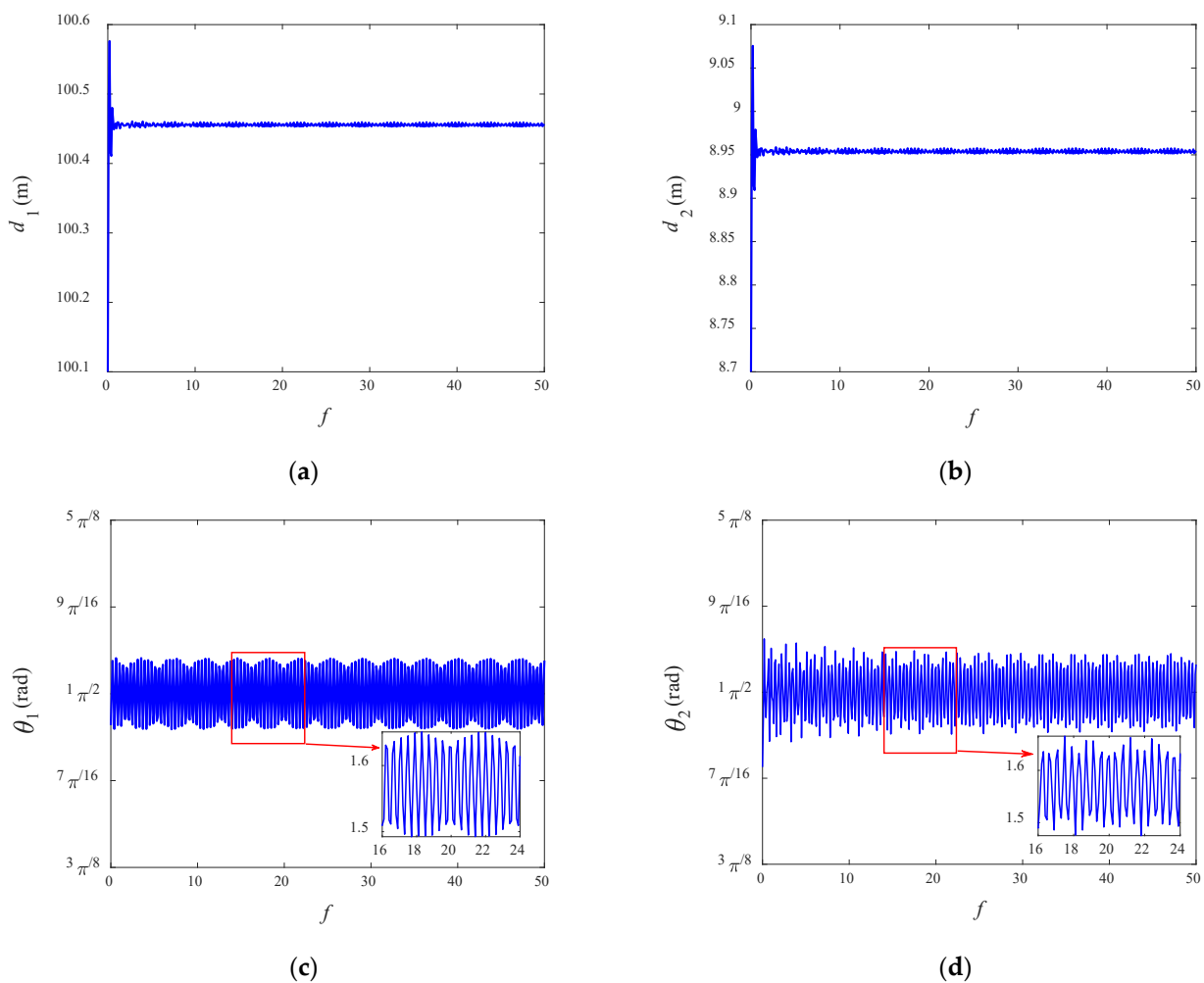


Figure 4. Variations of the generalized coordinates: (a) d_1 ; (b) d_2 ; (c) θ_1 ; (d) θ_2 .

It can be seen from Figure 5 that when the system moves towards the equilibrium state, the variations of tensions in the two segments of tethers show similar tendencies to d_1 and d_2 at the initial moment. When the equilibrium is reached, the tether tensions are also close to the value of F_{11e} and F_{12e} . They vary periodically with respect to f . As a result, the simulation results for equilibrium configuration support those of theoretical analysis as exhibited in Section 3.2.

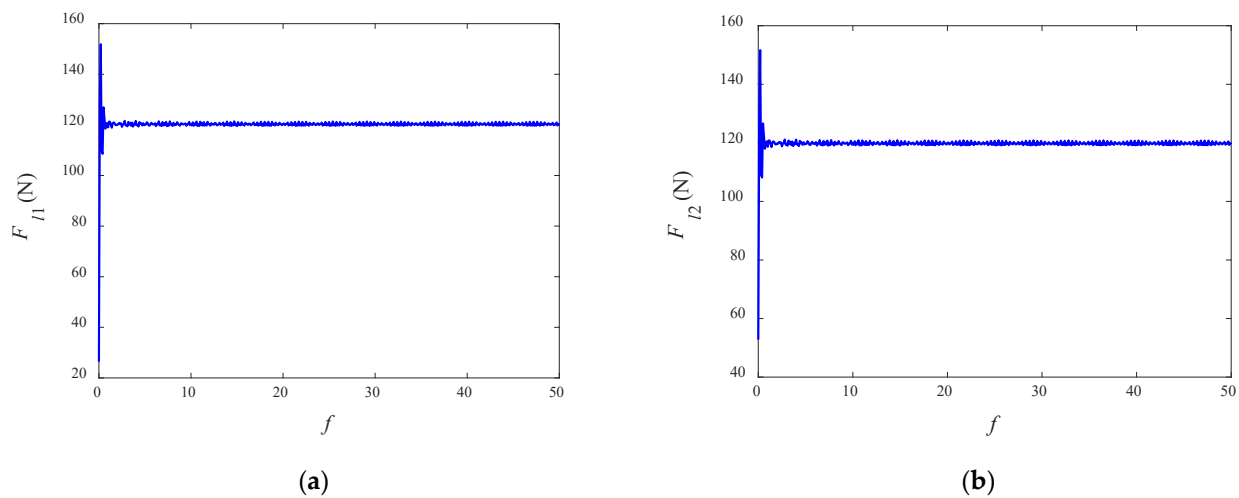


Figure 5. Variations of the tether tensions: (a) F_{l1} ; (b) F_{l2} .

5.2. Simulations for Libration Controller

As can be seen from the simulation results in Section 5.1, the changes of each generalized coordinate at the initial moment are obvious. The large libration amplitudes may result in additional fuel consumption and configuration failure. So, it is necessary to control the variations. To verify the effect of the libration controller, the controller parameters as selected as follows:

$$\begin{aligned} c_{s1} &= 10, \quad \varepsilon_{s1} = 0.01, \quad k_{s1} = 10 \\ c_{s2} &= 10, \quad \varepsilon_{s2} = 0.01, \quad k_{s2} = 10 \end{aligned} \quad (55)$$

Figure 6 shows the variations of generalized coordinates with the action of the designed controller. It can be seen from the figures that the system reaches the desired state at $f = 0.8$. The librations of the in-plane angles are effectively suppressed. Compared with the results in Figure 4, the in-plane angles are well maintained at $\pi/2$ to achieve the purpose of fuel saving. At the same time, the librations along the tether length at the initial moment are alleviated. It can be seen from Equations (9)–(12) that the in-plane angles and librations along the tether length are coupled with each other. When the former is suppressed, it is easy to stabilize the variations of the tether length.

Figure 7 shows the variations of the tethers' tension under the action of controller compared with the result of Figure 5. The variation trends are almost the same as those of d_1 and d_2 . This is due to the fact that when the system is in equilibrium, F_{l1} and F_{l2} are approximately the linear function of d_1 and d_2 whose slope is the stiffness coefficient of the tether.

The control results corresponding to those in Figures 6 and 7 are listed in Table 1. It can be seen from the table that the maximum values of the controlled variables after control are all smaller than those before control. This shows that the librations of the controlled variables are suppressed and the effectiveness of the libration controller is confirmed. In addition, it takes almost the same time for all the variables to approach the equilibrium state before and after control. On the other hand, adjusting the controller parameters can allow the system to reach the desired state faster.

Figure 8 shows the variations of the sliding mode surfaces. Figure 9 shows the variations of the control forces u_1 and u_2 . When s_1 and s_2 approach zero, θ_1 and θ_2 reach the desired state and the air jets stop working. It can be seen from Figure 9 that u_1 is positive and changes along the x_o -axis of the orbit frame while u_2 varies in the negative direction of the x_o -axis. To satisfy this control requirement and guarantee the desired performance, the tug and the sub-satellite are required to provide two opposing control torques to force the in-plane libration angles to the desired state.

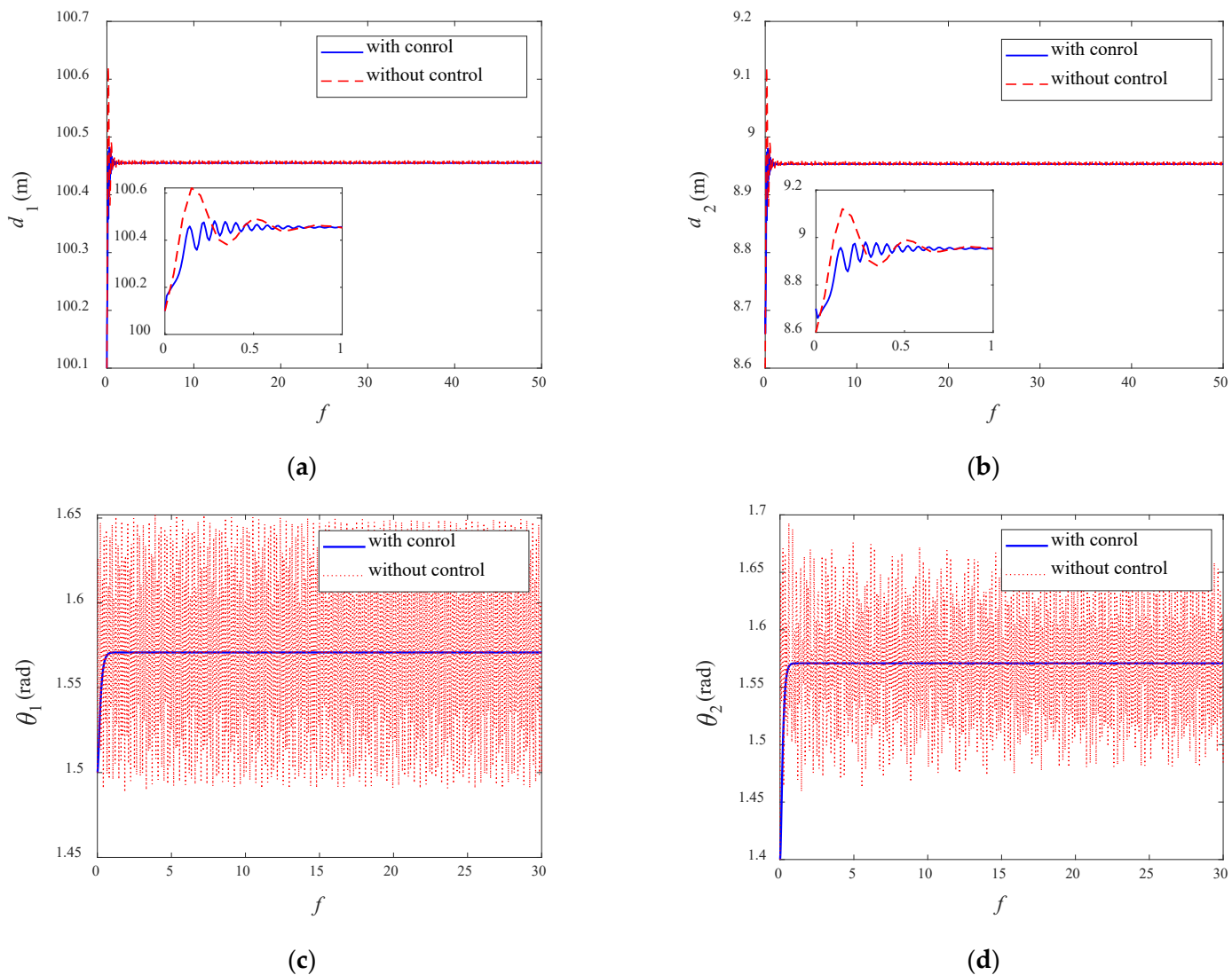


Figure 6. Variations of the generalized coordinates with and without control: (a) d_1 ; (b) d_2 ; (c) θ_1 ; (d) θ_2 .

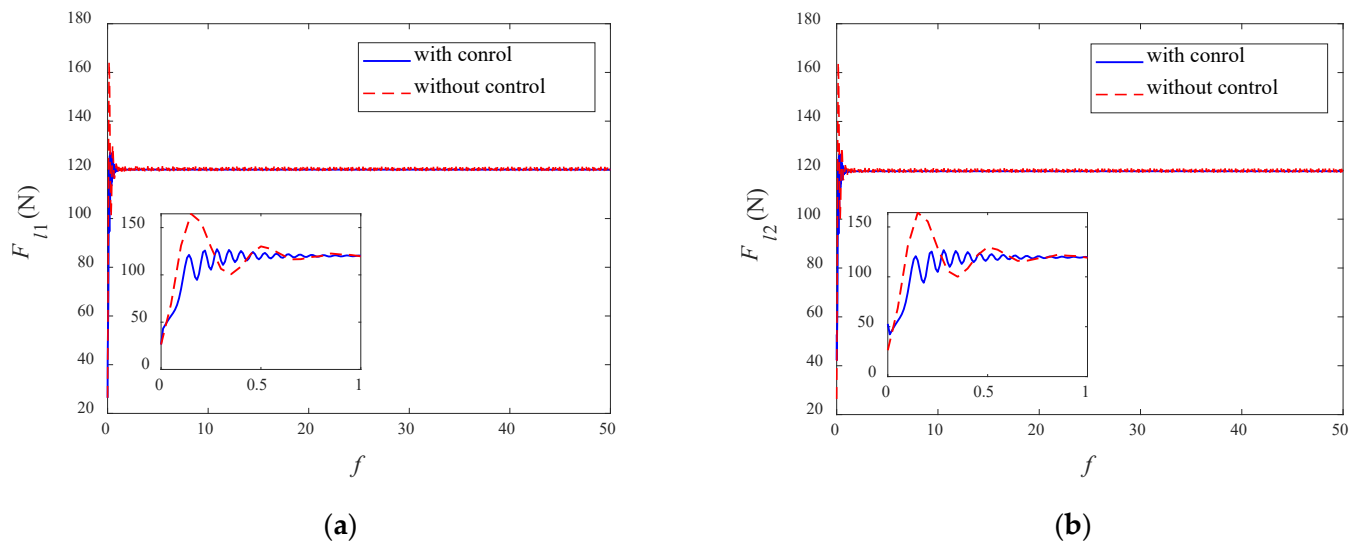


Figure 7. Variations of the tether tensions with and without control: (a) F_{11} ; (b) F_{12} .

Table 1. Performance comparison between the controlled variables before and after control.

Variables	Maximum Value without Control	Maximum Value with Control
d_1	100.621 (m)	100.482 (m)
d_2	9.121 (m)	8.980 (m)
θ_1	1.6519 (rad)	1.5708 (rad)
θ_2	1.6930 (rad)	1.5708 (rad)
F_{l1}	130.146 (N)	125.297 (N)
F_{l2}	129.745 (N)	124.850 (N)

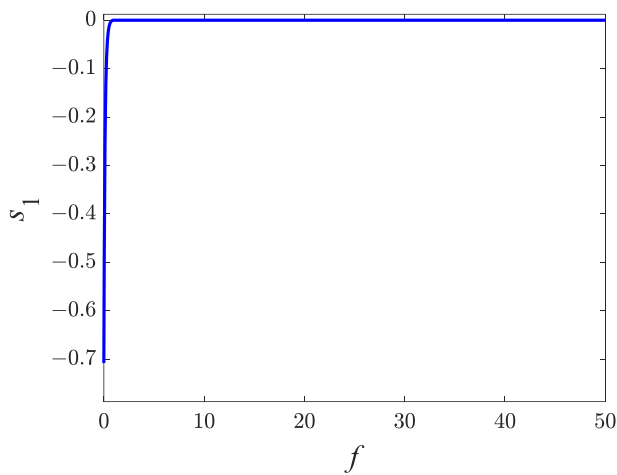
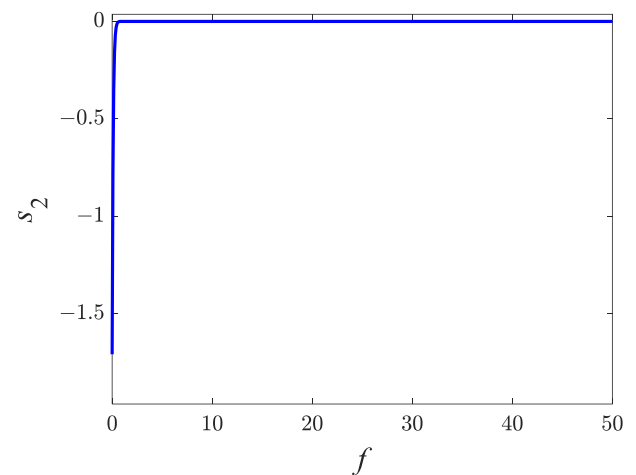
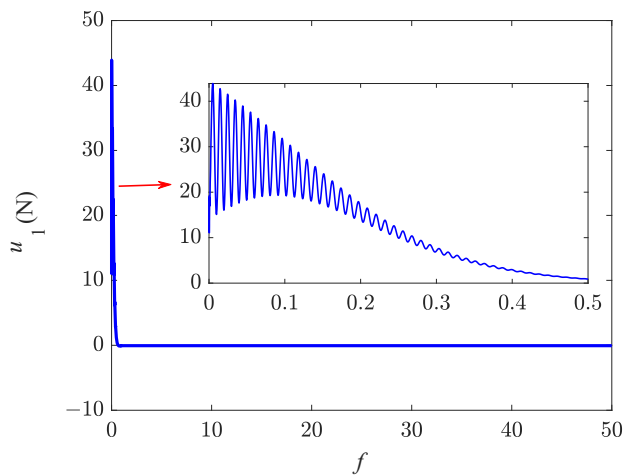
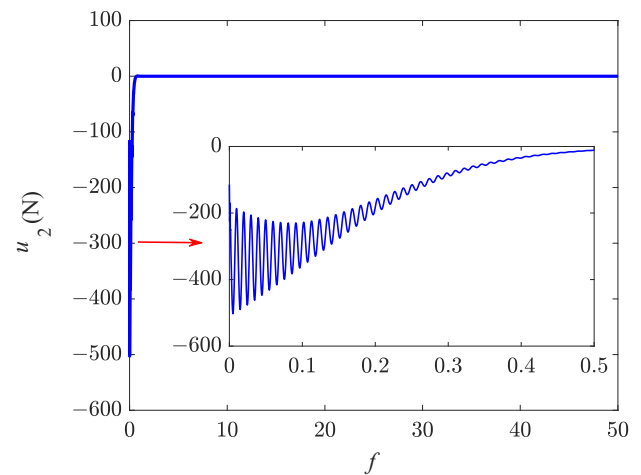
**(a)****(b)****Figure 8.** Variations of the sliding mode surfaces: (a) s_1 ; (b) s_2 .**(a)****(b)****Figure 9.** Variations of the control forces: (a) u_1 ; (b) u_2 .

Table 2 gives the statistical statements of Monte Carlo results about maximum control values and settling times. The random initial value range of each variable is set as $d_1 \in [99.8, 100.2]$, $d_2 \in [8.2, 8.8]$, $\theta_1 \in [1.4, 1.7]$, and $\theta_2 \in [1.4, 1.7]$. All the cases can converge within $f = 1.05$.

Table 2. Statistical statements of Monte Carlo results.

Number	Maximum Control Values (u_1)	Maximum Control Values (u_2)	Settling Time	Number	Maximum Control Values (u_1)	Maximum Control Values (u_2)	Settling Time
1	5.3113	2.7763	0.85	26	5.0009	4.3501	0.77
2	4.8808	2.6520	0.87	27	9.1271	3.7823	0.89
3	3.9296	1.6403	0.82	28	1.0997	4.3210	0.79
4	1.1259	2.9257	0.78	29	5.9695	3.4041	0.86
5	17.5118	2.6065	0.97	30	13.4755	3.6302	0.98
6	4.5052	2.6899	0.84	31	0.9988	4.3829	0.72
7	3.9099	2.1041	0.87	32	18.5756	4.1907	1
8	23.4981	2.8793	1.03	33	1.2196	4.2315	0.71
9	9.7099	3.6143	0.93	34	2.1536	4.1356	0.87
10	2.9807	2.9669	0.84	35	2.8406	3.5581	0.74
11	9.0193	1.7830	0.91	36	5.4548	2.1753	0.85
12	22.0454	3.8974	1.03	37	20.7834	2.2356	1
13	10.2877	1.0020	0.91	38	21.7675	3.8868	1.03
14	3.0421	3.9762	0.67	39	6.7766	3.8235	0.83
15	12.9003	3.2324	0.94	40	3.2731	2.4333	0.69
16	18.3562	3.5349	1	41	15.2439	2.4094	0.97
17	4.3885	2.5658	0.84	42	4.5732	3.3041	0.83
18	23.1578	2.1886	1.04	43	3.2812	2.1940	0.78
19	2.0496	2.8360	0.73	44	3.6449	4.2722	0.80
20	12.4655	1.3433	0.93	45	13.9039	3.0007	0.97
21	4.7030	1.6657	0.84	46	5.8025	3.1464	0.81
22	17.4816	2.0840	0.98	47	5.2472	3.6166	0.84
23	12.4809	1.1169	0.94	48	5.3351	3.9363	0.79
24	5.6282	1.9968	0.84	49	17.3646	2.7448	0.99
25	2.4166	2.1073	0.83	50	14.0092	2.4622	0.96

6. Conclusions

This paper develops a two-segment tethered towing system. A dynamic model is derived in the orbit frame. A set of equilibrium solutions are obtained based on the in-plane simplified model by considering the flexibility of the tethers. An in-plane libration controller is proposed by using the sliding mode control approach, where the equilibrium solution is taken as a desired state. Simulations with control and without control are performed to evaluate the performance of the controller. The following conclusions are drawn:

- (1) Seven sets of equilibrium configurations are given. The configuration in which the tug, sub-satellite, and debris remain in a straight line along the local horizontal is stable.
- (2) An in-plane libration controller is designed. According to the Lyapunov function, the system will converge to the sliding surface asymptotically. The system will reach the equilibrium asymptotically with the action of the designed libration controller. It can be seen from the Monte Carlo results that the control can converge within a short time.
- (3) It can be found from the simulation results that the librations in the direction of tether length can be effectively suppressed with the suppression of the oscillations of the in-plane angles. This is attributed to the coupling characteristics between in-plane angles and the tether length. As a result, the system under the action of the designed controller can reach the desired state while the librations of in-plane angles are effectively suppressed.

Author Contributions: Conceptualization, T.C. and J.K.; writing—original draft preparation, S.C.; writing—review and editing, S.C., W.C., T.C. and J.K.; visualization, S.C.; supervision, W.C. All authors have read and agreed to the published version of the manuscript.

Funding: This work was supported by the National Natural Science Foundation of China (Grant Nos. 12102174 and 12232011) and the Research Fund of State Key Laboratory of Mechanics and Control of Mechanical Structures (Nanjing University of Aeronautics and Astronautics) (Grant No. MCMS-I-0122K01).

Data Availability Statement: Not applicable.

Conflicts of Interest: The authors declare no conflict of interest.

References

1. Muelhaupt, T.J.; Sorge, M.E.; Morin, J.; Wilson, R.S. Space traffic management in the new space era. *J. Space Saf. Eng.* **2019**, *6*, 80–87. [[CrossRef](#)]
2. Shan, M.; Guo, J.; Gill, E. Deployment dynamics of tethered-net for space debris removal. *Acta Astronaut.* **2017**, *132*, 293–302. [[CrossRef](#)]
3. Botta, E.M.; Sharf, I.; Misra, A.K. Contact dynamics modeling and simulation of tether nets for space-debris capture. *J. Guid. Control Dyn.* **2017**, *40*, 110–123. [[CrossRef](#)]
4. Botta, E.M.; Sharf, I.; Misra, A.K.; Teichmann, M. On the simulation of tether-nets for space debris capture with vortex dynamics. *Acta Astronaut.* **2016**, *123*, 91–102. [[CrossRef](#)]
5. Benvenuto, R.; Lavagna, M.; Salvi, S. Multibody dynamics driving GNC and system design in tethered nets for active debris removal. *Adv. Space Res.* **2016**, *58*, 45–63. [[CrossRef](#)]
6. Sharf, I.; Thomsen, B.; Botta, E.M.; Misra, A.K. Experiments and simulation of a net closing mechanism for tether-net capture of space debris. *Acta Astronaut.* **2017**, *139*, 332–343. [[CrossRef](#)]
7. Yue, S.; Li, M.; Zhao, Z.; Du, Z.; Wu, C.; Zhang, Q. Parameter Analysis and Experiment Validation of Deployment Characteristics of a Rectangular Tether-Net. *Aerospace* **2023**, *10*, 115. [[CrossRef](#)]
8. Lv, S.; Zhang, H.; Zhang, Y.; Ning, B.; Qi, R. Design of an integrated platform for active debris removal. *Aerospace* **2022**, *9*, 339. [[CrossRef](#)]
9. Mark, C.P.; Kamath, S. Review of active space debris removal methods. *Space Policy* **2019**, *47*, 194–206. [[CrossRef](#)]
10. Stadnyk, K.; Ulrich, S. Validating the Deployment of a Novel Tether Design for Net-Based Orbital Debris Removal Missions. In Proceedings of the AIAA SciTech Forum and Exposition, Orlando, FL, USA, 6–10 January 2020; pp. 592–611.
11. Jung, W.; Mazzoleni, A.P.; Chung, J. Dynamic analysis of a tethered satellite system with a moving mass. *Nonlinear Dyn.* **2014**, *75*, 267–281. [[CrossRef](#)]
12. Abouelmagd, E.I.; Guirao, J.L.G.; Hobiny, A.; Alzahrani, F. Dynamics of a tethered satellite with variable mass. *Discret. Contin. Dyn. Syst. Ser. S* **2015**, *8*, 1035–1045. [[CrossRef](#)]
13. Abouelmagd, E.I.; Guirao, J.L.G.; Vera, J.A. Dynamics of a dumbbell satellite under the zonal harmonic effect of an oblate body. *Commun. Nonlinear Sci.* **2015**, *20*, 1057–1069. [[CrossRef](#)]
14. Pang, Z.; Jin, D.; Yu, B.; Wen, H. Nonlinear normal modes of a tethered satellite system of two degrees of freedom under internal resonances. *Nonlinear Dyn.* **2016**, *85*, 1779–1789. [[CrossRef](#)]
15. Aslanov, V.S.; Ledkov, A.S. Dynamics of towed large space debris taking into account atmospheric disturbance. *Acta Astronaut.* **2014**, *225*, 2685–2697. [[CrossRef](#)]
16. Aslanov, V.S.; Yuditsev, V.V. Dynamics, analytical solutions and choice of parameters for towed space debris with flexible appendages. *Adv. Space Res.* **2015**, *55*, 660–667. [[CrossRef](#)]
17. Aslanov, V.S.; Yuditsev, V.V. The motion of tethered tug–debris system with fuel residuals. *Adv. Space Res.* **2015**, *56*, 1493–1501. [[CrossRef](#)]
18. Aslanov, V.S.; Misra, A.K.; Yuditsev, V.V. Chaotic attitude motion of a low-thrust tug-debris tethered system in a keplerian orbit. *Acta Astronaut.* **2017**, *139*, 419–427. [[CrossRef](#)]
19. Aslanov, V.S.; Yuditsev, V.V. Chaos in tethered tug–debris system induced by attitude oscillations of debris. *J. Guid. Control Dyn.* **2019**, *42*, 1630–1637. [[CrossRef](#)]
20. Aslanov, V.S. Stability of a pendulum with a moving mass: The averaging method. *J. Sound Vib.* **2019**, *445*, 261–269. [[CrossRef](#)]
21. Lim, J.; Chung, J. Dynamic analysis of a tethered satellite system for space debris capture. *Nonlinear Dyn.* **2018**, *94*, 2391–2408. [[CrossRef](#)]
22. Shan, M.; Shi, L. Comparison of tethered post-capture system models for space debris removal. *Aerospace* **2022**, *9*, 33. [[CrossRef](#)]
23. Qi, R.; Misra, A.K.; Zuo, Z. Active debris removal using double-tethered space-tug system. *J. Guid. Control Dyn.* **2017**, *40*, 722–730. [[CrossRef](#)]
24. Hovell, K.; Ulrich, S. Attitude stabilization of an unknown and spinning target spacecraft using a visco-elastic tether. In Proceedings of the 13th Symposium on Advanced Space Technologies in Robotics and Automation, Noordwijk, The Netherlands, 11–13 May 2015; pp. 1–8.

25. Hovell, K.; Ulrich, S. Attitude stabilization of an uncooperative spacecraft in an orbital environment using visco-elastic tethers. In Proceedings of the AIAA Guidance, Navigation, and Control Conference, San Diego, CA, USA, 4–8 January 2016; pp. 1343–1358.
26. Hovell, K.; Ulrich, S. Experimental validation for tethered capture of spinning space debris. In Proceedings of the AIAA Guidance, Navigation, and Control Conference, Grapevine, TX, USA, 9–13 January 2017; pp. 626–644.
27. Hovell, K.; Ulrich, S. Postcapture dynamics and experimental validation of subtethered space debris. *J. Guid. Control Dyn.* **2018**, *41*, 519–525. [[CrossRef](#)]
28. Yang, K.Y.; Misra, A.K.; Zhang, J.; Qi, R.; Lu, S.; Liu, Y. Dynamics of a debris towing system with hierarchical tether architecture. *Acta Astronaut.* **2020**, *177*, 891–905. [[CrossRef](#)]
29. Abouelmagd, E.I.; Guirao, J.L.G.; Hobiny, A.; Alzahrani, F. Stability of equilibria points for a dumbbell satellite when the central body is oblate spheroid. *Discret. Contin. Dyn. Syst. S* **2015**, *8*, 1047–1054. [[CrossRef](#)]
30. Hu, W.; Song, M.; Deng, Z. Energy dissipation/transfer and stable attitude of spatial on-orbit tethered system. *J. Sound Vib.* **2018**, *412*, 58–73. [[CrossRef](#)]
31. Lian, X.; Liu, J.; Zhang, J.; Wang, C. Chaotic motion and control of a tethered-sailcraft system orbiting an asteroid. *Commun. Nonlinear Sci. Numer. Simul.* **2019**, *77*, 203–224. [[CrossRef](#)]
32. Liu, J.F.; Qu, W.L.; Yuan, L.H.; Cui, N.G. Nonlinear dynamics of a space tethered system in the elliptic earth-moon restricted three-body system. *J. Aerosp. Eng.* **2019**, *32*, 04018139. [[CrossRef](#)]
33. Sun, L.; Zhao, G.; Huang, H. Effect of mass variation on dynamics of tethered system in orbital maneuvering. *Acta Astronaut.* **2018**, *146*, 15–23. [[CrossRef](#)]
34. Jin, D.P.; Hu, H.Y. Optimal control of a tethered subsatellite of three degrees of freedom. *Nonlinear Dyn.* **2006**, *46*, 161–178. [[CrossRef](#)]
35. Sun, X.; Zhong, R. Switched propulsion force libration control for the low-thrust space tug system. *Aerosp. Sci. Technol.* **2018**, *80*, 281–287. [[CrossRef](#)]
36. Wen, H.; Zhu, Z.H.; Jin, D.; Hu, H. Constrained tension control of a tethered space-tug system with only length measurement. *Acta Astronaut.* **2016**, *119*, 110–117. [[CrossRef](#)]
37. Zhang, Z.; Yu, Z.; Zhang, Q.; Zeng, M.; Li, S. Dynamics and control of a tethered space-tug system using Takagi-Sugeno fuzzy methods. *Aerosp. Sci. Technol.* **2019**, *87*, 289–299. [[CrossRef](#)]
38. Zhang, J.; Yang, K.; Qi, R. Dynamics and offset control of tethered space-tug system. *Acta Astronaut.* **2018**, *142*, 232–252. [[CrossRef](#)]
39. Kang, J.; Zhu, Z.H.; Santaguida, L.F. Analytical and experimental investigation of stabilizing rotating uncooperative target by tethered space tug. *IEEE Trans. Aerosp. Electron. Syst.* **2021**, *57*, 2426–2437. [[CrossRef](#)]
40. Razzaghi, P.; Al Khatib, E.; Bakhtiari, S. Sliding mode and SDRE control laws on a tethered satellite system to de-orbit space debris. *Adv. Space Res.* **2019**, *64*, 18–27. [[CrossRef](#)]
41. Chu, Z.; Di, J.; Cui, J. Hybrid tension control method for tethered satellite systems during large tumbling space debris removal. *Acta Astronaut.* **2018**, *152*, 611–623. [[CrossRef](#)]
42. Xu, S.; Sun, G.; Ma, Z.; Li, X. Fractional-order fuzzy sliding mode control for the deployment of tethered satellite system under input saturation. *IEEE Trans. Aerosp. Electron. Syst.* **2018**, *55*, 747–756. [[CrossRef](#)]
43. Xu, S.; Wen, H.; Huang, Z.; Jin, D. A fuzzy control scheme for deployment of space tethered system with tension constraint. *Aerosp. Sci. Technol.* **2020**, *106*, 106143. [[CrossRef](#)]
44. Kang, J.; Zhu, Z.H.; Wang, W.; Li, A.; Wang, C. Fractional order sliding mode control for tethered satellite deployment with disturbances. *Adv. Space Res.* **2017**, *59*, 263–273. [[CrossRef](#)]
45. Li, X.; Sun, G.; Shao, X. Discrete-time pure-tension sliding mode predictive control for the deployment of space tethered satellite with input saturation. *Acta Astronaut.* **2020**, *170*, 521–529. [[CrossRef](#)]
46. Li, X.; Sun, G.; Han, S.; Shao, X. Fractional-order nonsingular terminal sliding mode tension control for the deployment of space tethered satellite. *IEEE Trans. Aerosp. Electron. Syst.* **2021**, *57*, 2759–2770. [[CrossRef](#)]
47. Li, X.; Sun, G.; Xue, C. Fractional-order deployment control of space tethered satellite via adaptive super-twisting sliding mode. *Aerosp. Sci. Technol.* **2022**, *121*, 107390. [[CrossRef](#)]
48. Liu, E.; Yang, Y.; Yan, Y. Spacecraft attitude tracking for space debris removal using adaptive fuzzy sliding mode control. *Aerosp. Sci. Technol.* **2020**, *107*, 106310. [[CrossRef](#)]
49. Khalil, H.K. *Nonlinear Control*, 3rd ed.; Pearson: New York, NY, USA, 2015; pp. 133–139.

Disclaimer/Publisher’s Note: The statements, opinions and data contained in all publications are solely those of the individual author(s) and contributor(s) and not of MDPI and/or the editor(s). MDPI and/or the editor(s) disclaim responsibility for any injury to people or property resulting from any ideas, methods, instructions or products referred to in the content.